

Effects of single circular synthetic jet on turbulent boundary layer

Jinhao Zhang

Tianjin University

Biao-Hui Li

Tianjin University

Nan Jiang (✉ nanj@tju.edu.cn)

Tianjin University

Research Article

Keywords: synthetic jet, hairpin vortex, drag reduction, turbulent boundary layer

Posted Date: July 27th, 2022

DOI: <https://doi.org/10.21203/rs.3.rs-1866775/v1>

License: © ⓘ This work is licensed under a Creative Commons Attribution 4.0 International License.

[Read Full License](#)

Effects of single circular synthetic jet on turbulent boundary layer

Jin-Hao Zhang(张津浩)^{1,a)}, Biao-Hui Li(李彪辉)¹, Nan Jiang(姜楠)^{1,2,b)}

¹*Department of Mechanics, School of Mechanical Engineering, Tianjin University, Tianjin 300350, China*

²*Tianjin Key Laboratory of Modern Engineering Mechanics, Tianjin 300350, China*

The periodic synthetic jet emerging from a circular hole actively controls the turbulent boundary layer (TBL). A time-resolved particle image velocimetry (TR-PIV) system was designed to capture the velocity field database and based on the single-pixel ensemble correlation (SPEC) algorithm, an average drag reduction rate of 6.2% was obtained. The results show that the synthetic jet causes a wide range of low momentum zones and a low-speed streak in the downstream flow field. And the places where the disturbance intensity is strong are often accompanied by a larger velocity deficit. The instantaneous flow fields are visualized with the Finite-Time Lyapunov Exponent (FTLE), and the hairpin vortex packet composed of five hairpin vortices and the generation of new hairpin vortices are observed when there is no control. Under the action of the synthetic jet, the hairpin vortices are continuously generated from the jet hole. The synthetic jet mainly achieves the drag reduction effect mainly by modulating the mean convection term c^C and the spatial development term c^D . The drag reduction effect appears in the region of $x/\delta_0 > 0.38$, and the maximum drag reduction rate is 12.2% at $x/\delta_0 = 0.75$, and then gradually decreased. Using proper orthogonal decomposition (POD), it is found that the synthetic jet reduces the energy proportion of the large-scale energetic structures. After the conditional average, the synthetic jet limits the influence range of bursting events at various scales in the near-wall region, and weakens the normal transport of momentum and energy brought about by large-scale ejection events (Q2 events) and the wall friction resistance caused by large-scale sweep events (Q4 events).

Keywords: synthetic jet, hairpin vortex, drag reduction, turbulent boundary layer

PACS: 47.85.lb, 47.85.ld, 47.27.nb, 47.27.De

1 Introduction

There are many types of coherent structures in TBL, and the vortex structure is the main one. Robinson (1991) applied the following definition of a vortex structure: Viewed in a Lagrangian reference frame, a vortex exists when the clockwise streamlines projected onto a plane perpendicular to the vortex core axis exhibit a roughly circular or helical pattern. The vortex structure he defined does not exist instantaneously, but means that fluid structures move together for a finite time. Many kinds of vortex

^{a)} Email: zhangjh0625@outlook.com

^{b)} Author to whom correspondence should be addressed: nanj@tju.edu.cn

identification criteria have been proposed aiming at the precise mathematical definition of vortex, and each one has its specific scope of application, so these are not universal. The more common identification methods are as follows: Q criterion (Hunt et al. 1988), λ_2 criterion (Jeong and Hussain 1995), Δ criterion (Chong et al. 1990), λ_{ci} criterion (Zhou et al. 1999), etc. These are all identification formats based on the velocity gradient tensor ∇u , which require the given velocity field to have a high spatial resolution. In addition, the above methods based on the Euler coordinate system lack objectivity: the threshold value near the zero point is usually selected to judge the boundary of the vortex structure, which brings subjectivity. In recent years, Haller and Yuan (2000) made an attempt to identify vortices under the Lagrangian system, and proposed a new criterion: the Finite-Time Lyapunov Exponent. The structure obtained with FTLE is called the Lagrangian coherent structure (LCS). Voth et al. (2002) used FTLE to process temporally periodic experimental data. Mathur et al. (2007) applied FTLE to turbulent experimental data to identify LCS in two-dimensional turbulent flow. Shadden et al. (2005) studied the flow properties at the boundary of the vortex ring by FTLE. Subsequently, Green et al. (2007) identified a horseshoe-shaped LCS in the DNS data of the channel flow, and this coherent structure is also known as the hairpin vortex.

In order to study the hairpin vortex, based on its generation mechanism (Kim et al. 1971), the artificial hairpin vortex technology had gradually developed. Acarlar and Smith (1987-2) proposed to generate hairpin vortices by creating artificial low-velocity streak regions in the laminar boundary layer. Meanwhile, Acarlar and Smith (1987-1) found that the interaction with a hemispheric protrusion in the boundary layer can generate hairpin vortices. Later, Tang and Jiang (2012) also verified their conclusion. Through numerical studies, Saponitsky et al. (2005) established a model for the interaction of local perturbation (synthetic jet) and laminar base flow, and found that the synthetic jet could shear in a fully developed TBL to form hairpin vortices.

The synthetic jet is generated by the actuator, which is mainly composed of cavity, vibrating membrane and jet hole. (Smith and Glezer 1998) When the synthetic jet actuator (SJA) works, the reciprocating movement of the vibrating membrane under the

condition of electricity causes the pressure in the cavity to change periodically, thus producing blowing and sucking fluid movement at the jet hole. With the development of technology, there are many different vibration modes of SJA, such as piston type (Gilarranz et al. 2002), piezoelectric membrane type (Rathnasingham and Breuer 1997), electromagnetic excitation type (Lasagna et al. 2014) and so on. Park et al. (2003) conducted an experimental study on the influence of periodic synthetic jets on TBL, and the results of phase average shown that large-scale spanwise vortices would be generated downstream of the slit, which was called hairpin vortex head. It was found that the synthetic jet also had drag reduction effect, and the drag reduction intensity was different at different flow direction.

Rathnasingham and Breuer (2003) experimentally researched the active control of the synthetic jet on TBL and found that it minimized the streamwise velocity fluctuation by 30% at a certain position downstream of the actuator, while the wall pressure fluctuation and average wall shear stress were correspondingly reduced. Ye et al. (2019) conducted loop-opening control of TBL by using the synthetic jet array in the experiment, and the results showed that the synthetic jet array had drag reduction effect on TBL within a certain distance downstream. The perturbation intensity of the synthetic jet attenuated along the streamwise direction, and the perturbation was mainly concentrated in the logarithmic region and extended to the outer region of TBL, which could obviously change the flow field structure of TBL. Lu et al. (2020) used circular synthetic jet array to control the fully developed TBL. Their research exhibited that that the injection of synthetic jet effectively suppressed the bursting events intensity of turbulence in the near-wall region and the lifting effect of synthetic jet increased the normal height of streamwise vortex. Berk et al. (2018) found that the entry of synthetic jet into TBL would lead to local momentum deficit in TBL, which was mainly due to the vortex structure generated by the interaction between TBL and the synthetic jet. Glezer and Amitay (2002) proposed that a single synthetic jet was generated by the interaction of a series of vortices, which were usually formed by alternating instantaneous blowing and sucking of fluid through the jet hole.

Fukagata et al. (2002) derived an exact mathematical expression (Fukagata-Lwamoto-Kasagi identity, FIK identity) for the contribution of different dynamic effects to the frictional drag components in turbulent channel, pipe and spatial boundary layer flows. The FIK identity decomposes the local wall friction into four distinct dynamic contributions, namely laminar, turbulent, inhomogeneous and transient components, and the second part is the weighted integral of the Reynolds stress distribution. The FIK identity had been utilized to quantify the contribution of Reynolds stress to wall friction in compressible (Gomez et al. 2009) and incompressible (Fukagata and Kasagi 2002) fluids, as well as to quantitatively discuss the drag reduction mechanisms for TBLs such as active control (Fukagata and Kasagi 2003), riblets (Peet and Sagaut 2009), polymer or surfactant addition (Yu et al. 2004; Hou et al. 2008), and microbubbles (Xu et al. 2007; Sugiyama et al. 2008). In addition, the FIK identity is also used to design new control schemes (Min et al. 2006). Fukagata and Kasagi (2004) presented a new sub-optimal wall turbulent drag reduction control law and the results of direct numerical simulation (DNS) showed that the control law could effectively reduce the frictional resistance in the pipeline. Mehdi and white (2011) proposed an integral method, replacing the streamwise direction gradient with the wall-normal total stress gradient, for calculating the friction coefficient of the boundary layer flow surface, which is useful in situations where measurements at multiple streamwise direction locations are not available or feasible.

In the present study, based on previous research results, a single circular synthetic jet experiment is designed and TR-PIV system is utilized to record flow field information. We discuss the distribution characteristics of the synthetic jet disturbance and try to visualize the hairpin vortex generated by the jet using FTLE method. Then, we use FIK identity and SPEC algorithm to verify the local effect of drag reduction. And the drag reduction mechanism of the synthetic jet is studied. This article is divided into four sections. Section 2 introduces the experimental settings, measurement methods, and the boundary layer parameters. Section 3 exhibits results obtained from the measure via TR-PIV. Finally, Section 4 presents the concluding remarks.

2 Experimental details

2.1 Experimental facility

The experiment was carried out in a low-speed reflux water channel in the Fluid Mechanics Laboratory of Tianjin University. The channel was semi-enclosed with an upper opening and contained an experimental section of $6.20\text{m} \times 0.29\text{m} \times 0.38\text{m}$ (length \times width \times height, as shown in Fig.1(a)). The sides and underside of the channel test section are plexiglass and allowed optical access.

The experimental study was mainly divided into two parts, including the measurement of TBL on the classical smooth horizontal plate and the measurement of TBL when the synthetic jet was applied. Each part measured the flow field in the streamwise-wall-normal plane and the streamwise-spanwise plane. Fig.1(a) and 1(b) show the 3D images of experimental settings in the shooting process of the two planes respectively. In this experiment, when the free-stream velocity $U_\infty = 0.255\text{m/s}$, the corresponding background turbulence was less than 1.5%, and the coefficient of kinematic viscosity of water was $\nu = 9.6 \times 10^{-7}\text{m}^2/\text{s}$. A smooth plate which was 2.9m long, 0.25m wide and 0.02m thick was placed horizontally in the experimental section of the channel, and had a 4:1 (long: short) semi-oval leading edge. TBLs were developed on the plate and a trip wire with a diameter of 2mm was fixed at 0.2m downstream of the leading edge to stimulate the production of the full-developed TBL. A 4mm diameter circular hole was made at the center line 2.45m from the leading edge and was connected with a cavity with a diameter of 38mm. At the bottom of the plate, an actuator was placed under the cavity. Given a sinusoidal signal of a fixed voltage and frequency (10V and 26Hz in the research, this condition had the best drag reduction effect, for the sake of the drag reduction mechanism of synthetic jet), it periodically generated the synthetic jet from the hole. Parameters of the cavity and the placement of the actuator are rendered in Fig.1(c). In this paper, the streamwise direction, wall-normal direction and spanwise direction are represented by x , y , z . Accordingly, the instantaneous velocity and fluctuation velocity in the three directions are given by u ,

v , w and u' , v' , w' , respectively. The streamwise and spanwise position at the center of the hole are defined as $x = 0$ and $z = 0$, and the wall-normal location of the upper surface of the plate is $y = 0$.

A TR-PIV system was utilized to collect the instantaneous velocity field. The water surface in the flume was 0.2m higher than the upper surface of the plate, and the polyamide particles with an average diameter of $20\mu\text{m}$ and a density of $1.03\text{g}/\text{mm}^3$ similar to water were evenly distributed in the flow. The experimental section was illuminated with a 1mm thick continuous laser sheet, and the specific plane being studied could be determined by focusing the camera lens. In order to avoid laser reflection, the part of the plate illuminated by laser is blackened.

Table 1 The parameters of two cameras

Variables	Camera #1	Camera #2
Focal length of lens	60mm	200mm
Resolution	1280 × 800 pixels	1280 × 800 pixels
Sampling frequency	360Hz	360Hz
Number of snapshots	41080	41080
Field of view	107mm × 67mm	26.06mm × 1.63mm
Particle density	23 per 32 × 32 pixels	16 per 64 × 64 pixels
Left edge position	$x = -15\text{mm}$	$x = 15\text{mm}$

When the streamwise-wall-normal plane ($x - y$ plane) was photographed, the laser sheet through the orifice illuminated the flow field vertically downwards parallel to the streamwise direction. Two Speed Sense 9072 12-bit charge-coupled device (CCD) (camera #1 and camera #2) took images from the side perpendicular to the laser sheet. When the streamwise-spanwise plane ($x - z$ plane) was measured, the laser sheet was parallel to the plate to illuminate the flow field from the side. At this point, the shooting plane was about 4.5mm away from the upper surface of the plate ($h = 4.5\text{mm}$). Camera #1 collected images perpendicular to the laser plane. The parameters of the two cameras are listed in Table 1. The field of view (FOV) acquired by camera #1 was large and the

iterative multi-grid cross-correlation algorithm was used to transform the images into the corresponding speed field. The query windows were set to $32 \text{ pixels} \times 32 \text{ pixels}$ and the overlap rate was 75%, so that the distance between adjacent speed vectors obtained was 0.69mm. Camera #2 used a longer focal length lens to acquire images of the near-wall region with a spatial resolution of 0.0204mm/pixel, and SPEC (Westerweel et al. 2004; Shen et al. 2014) algorithm was utilized to calculate the mean velocity profile. The whole flow field was analyzed through the images captured by camera #1, and the wall friction velocity was fitted by the image taken by camera #2.

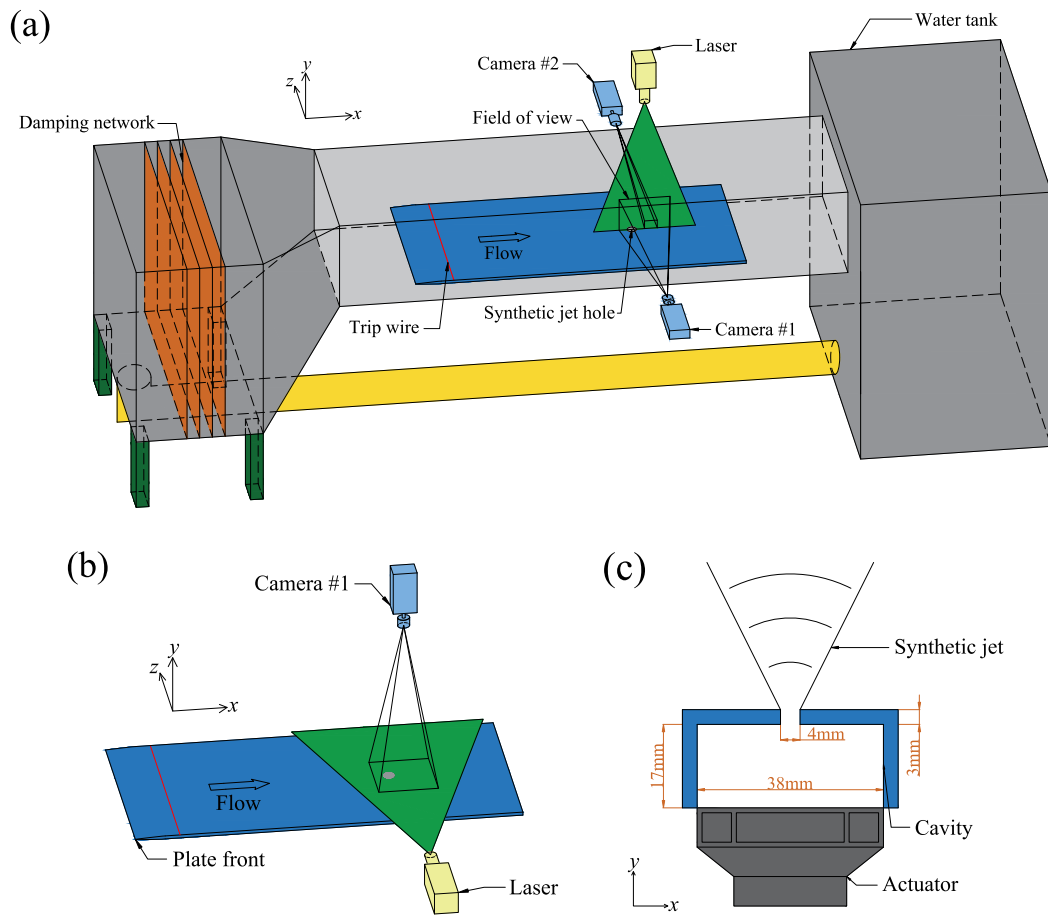


FIG. 1 Schematic diagram of experimental setup: (a) Streamwise-wall-normal plane shooting; (b) Streamwise-spanwise plane shooting; (c) Details of cavity and actuator

2.2 Flow basic parameters

Table 2 describes the flow parameters of TBL with non-control (00V 00Hz) when TBL is fully developed. For the velocity fields calculated by the large FOV, the wall friction velocity fitted by Spalding profile (Kendall and Koochesfahani 2008) which is

expressed as

$$y^+ = u^+ + e^{-\kappa B} [e^{\kappa u^+} - 1 - \kappa u^+ - (\kappa u^+)^2/2 - (\kappa u^+)^3/6]$$

is $u_\tau = 11.21\text{mm/s}$, where $\kappa = 0.41$ and $B = 5.2$ are the log-law constants. For the results of SPEC, $u_\tau = 11.22\text{mm/s}$ is obtained by linear law fitting. The fitting errors of the two methods are less than 1%, and the results acquired are consistent basically. After that, $u_\tau = 11.21\text{mm/s}$ will be utilized as the standard value.

Table 2 Flow parameters of boundary layer

Parameters	Values
Free-stream velocity U_∞ (mm/s)	255
Friction velocity u_τ (mm/s)	11.21
Skin friction stress (kg/(m·s ²))	0.1255
Skin friction coefficient C_f	3.86×10^{-3}
Boundary layer thickness δ_0 (mm)	46.0
Displacement thickness δ^* (mm)	6.41
Momentum thickness δ_θ (mm)	4.98
Shape factor H	1.29
Friction velocity Re number Re_τ	537

The nominal boundary layer thickness δ_0 depends on the wall-normal position of $0.99U_\infty$. The wall friction stress is defined as

$$\tau_w = \rho u_\tau^2.$$

Accordingly, the wall friction coefficient can be described as

$$C_f = 2\tau_w/\rho u_\infty^2 = 2u_\tau^2/u_\infty^2.$$

Finally, the drag reduction rate is obtained as follows

$$DR = (1 - C_{f1}/C_{f0}) \times 100\%.$$

In the formula, “1” in the lower right corner represents exerting control, while “0” represents not exerting control.

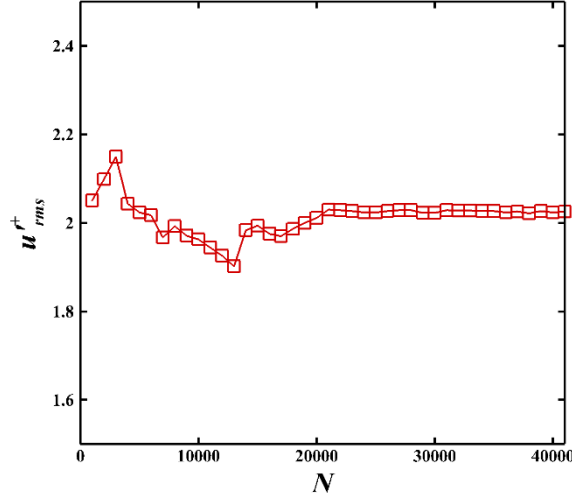


FIG. 2 Verification of convergence of second-order statistics

Because the perturbation of the synthetic jet is not as uniform as that of passive control, the velocity profile in the logarithmic region produces distortion. However, due to the strong viscous effect of the fluid near the wall, the flow in the viscous sublayer is more stable than that in other regions and the data obtained by SPEC is utilized to fit u_τ . At last, the relevant results calculated after control are as follows: $\tau_w = 0.1178$ kg/(m·s²), $C_{f1} = 3.63 \times 10^{-3}$, $DR = 6.2\%$. It can be seen that an average drag reduction rate of 6.2% is acquired in the range of $x = 15\text{mm} \sim 26\text{mm}$ under the effect of the synthetic jet.

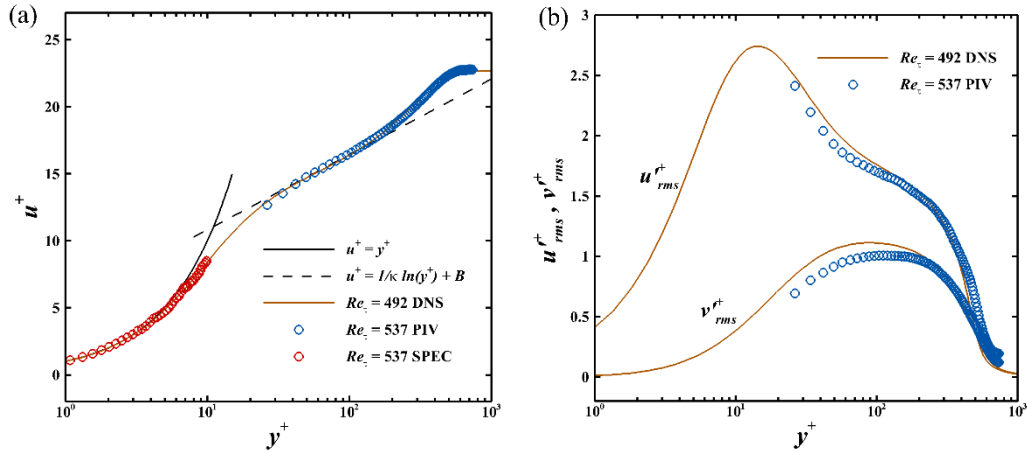


FIG. 3 Profiles of (a) mean streamwise velocity and (b) root mean square (RMS) of streamwise and wall-normal fluctuation velocity

Fig.2 illustrates the dependence of second-order quantities at position $x = 0$, $y = 3.58\text{mm}$, $z = 0$ on statistical sample N . $u'_{rms}+$ shows a convergence trend when $N > 21000$ approximately, indicating that the sample number measured by PIV is

sufficient for statistical analysis of time-homogeneity characteristics and fluctuation characteristics. In the figure, velocity and length, identified by “+”, are dimensionless with internal scale units u_τ (friction velocity) and $\frac{u_\tau}{\nu}$ (viscous wall units) respectively.

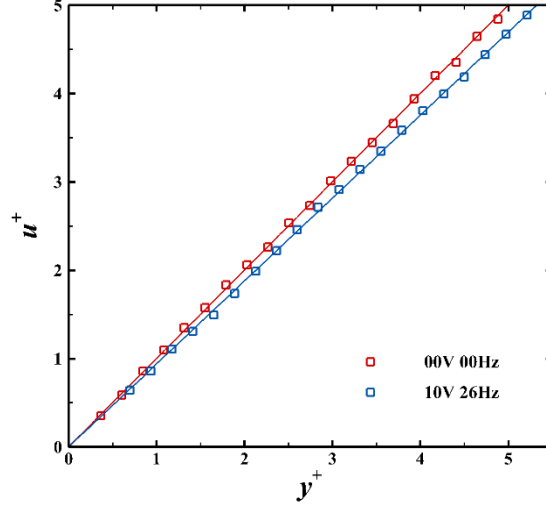


FIG. 4 Mean streamwise velocity profile of viscous sublayer

Fig.3 demonstrates the average velocity profile and fluctuation intensity profile measured in the experiment, and the DNS data of zero pressure gradient TBL under similar Reynolds number acquired by Schlatter and Orlu (2010) is added for comparison. It can be seen that the two sets of data are basically consistent, which indicates that a fully developed TBL has been obtained for the next experiment. Fig.4 describes the streamwise velocity profiles of the viscous bottom layer under the two conditions. It can be found that the slope of the curve is lower and the viscous sublayer is thicker with the control of synthetic jet, which is a typical feature to reduce the friction resistance.

3 Results and discussion

3.1 The intensity of disturbance

After the flow field is controlled by synthetic jet, the efflux flows vertically into TBL along the wall-normal direction at the outlet position, and it has less energy and momentum on the streamwise direction, so that it will have a violent exchange of energy and momentum with the incoming flow, resulting in a wide range of low-speed regions (Lardeau and Leschziner 2011).

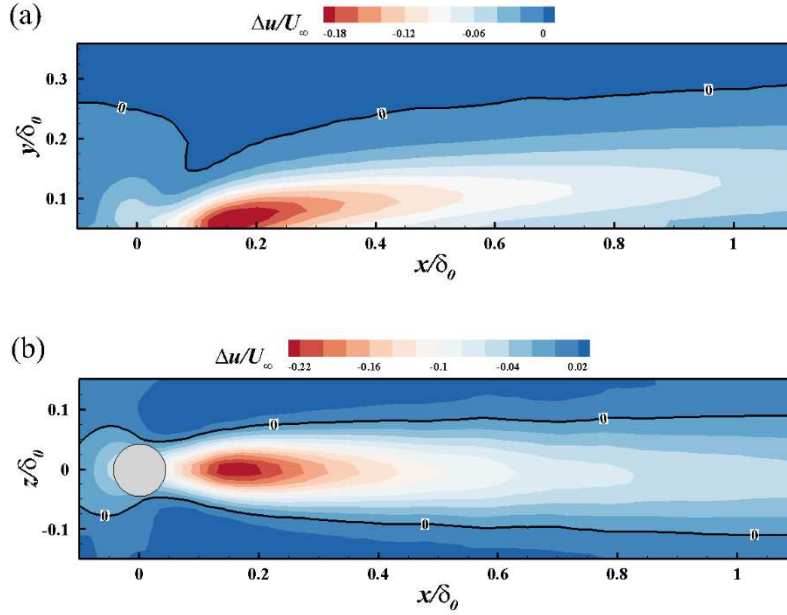


FIG. 5 The contours of the difference between controlled and uncontrolled time-averaged streamwise velocity in (a) $x - y$ plane and (b) $x - z$ plane

Fig.5(a) and 5(b) show the nephograms of the difference in streamwise velocity between controlled and uncontrolled flow in the streamwise-wall-normal plane and streamwise-spanwise plane respectively. The solid black lines are zero contour lines, while jet hole is marked by gray area. It can be observed from Fig.5(a) that a large area of velocity loss occurs in the downstream of the jet hole, while the upstream is also slightly affected. The velocity isolines appear to be inclined ellipses, which means that the speed deficit reaches its maximum value around $x/\delta_0 = 0.175$ and then decreases downstream. Meanwhile, the height of zero contour line gradually increases with the downstream, and at the height above the 0 contour, the streamwise velocity increases slightly. In Fig.5(2), the velocity deficit region at height $y/\delta_0 = 0.098$ presents a symmetrical shape along $z/\delta_0 = 0$, and extends to the both sides with the streamwise direction, which indicates that a low-speed streak is generated in the downstream flow field by the synthetic jet. The width of the low-speed streak is narrowest near the orifice and gradually increases downstream.

The synthetic jet makes the flow field appear velocity deficit area, so there is a certain relationship between the disturbance intensity and deficit value. The flow field

controlled by the synthetic jet can be regarded as a signal with a fixed frequency (26Hz) noise. At this point, if the velocity signal is converted to the frequency signal, the noise at this frequency can represent the disturbance of the jet, which is completed by using the Fourier transform.

The Formula for the Fourier transform is obtained according to

$$F(f) = \mathcal{F}[u(t)] = \int_{-\infty}^{\infty} u(t)e^{-ift} dt,$$

where f , t and e^{-ift} represent frequency, time and complex function respectively. Fourier transform considers that a periodic function (signal) contains multiple frequency components, and any function (signal) $u(t)$ can be synthesized by adding multiple periodic function (basis functions). From the physical point of view, the Fourier transform is the linear transformation of the original function with a set of special functions (trigonometric functions) as an orthogonal basis, and the physical meaning is the projection of the original function in each group of basis functions.

A section of $u(t)$ when $|t| \leq \frac{T}{2}$ is taken to obtain a truncation function $u_T(t)$, which can be expressed as

$$u_T(t) = \begin{cases} u(t) & (|t| \leq \frac{T}{2}) \\ 0 & (|t| > \frac{T}{2}) \end{cases}.$$

If T is finite, then $u_T(t)$ has finite energy. Given: $\mathcal{F}[u_T(t)] = F_T(f)$. In this case, since the energy in the time domain is equal to that in the frequency domain, the energy E_T of $u_T(t)$ can be described as

$$E_T = \int_{-\infty}^{\infty} u_T^2(t) dt = \frac{1}{2\pi} \int_{-\infty}^{\infty} |F_T(f)|^2 df.$$

Due to

$$\int_{-\infty}^{\infty} u_T^2(t) dt = \int_{-T/2}^{T/2} u^2(t) dt,$$

the average power P is

$$P = \lim_{T \rightarrow \infty} \int_{-T/2}^{T/2} \frac{1}{T} u^2(t) dt = \frac{1}{2\pi} \int_{-\infty}^{\infty} \lim_{T \rightarrow \infty} \frac{1}{T} |F_T(f)|^2 df.$$

The power spectral density (PSD) $P(f)$ of $u(t)$ is

$$P(f) = \lim_{T \rightarrow \infty} \frac{1}{T} |F_T(f)|^2.$$

$P(f)$ is an even function, also known as the bilateral power spectrum. To make the total power conserved, the unilateral power spectrum is always twice the bilateral power spectrum: $S(f) = 2P(f)$. In engineering, it is customary to take $10 \log_{10} S(f)$ and the unit is: dB/Hz.

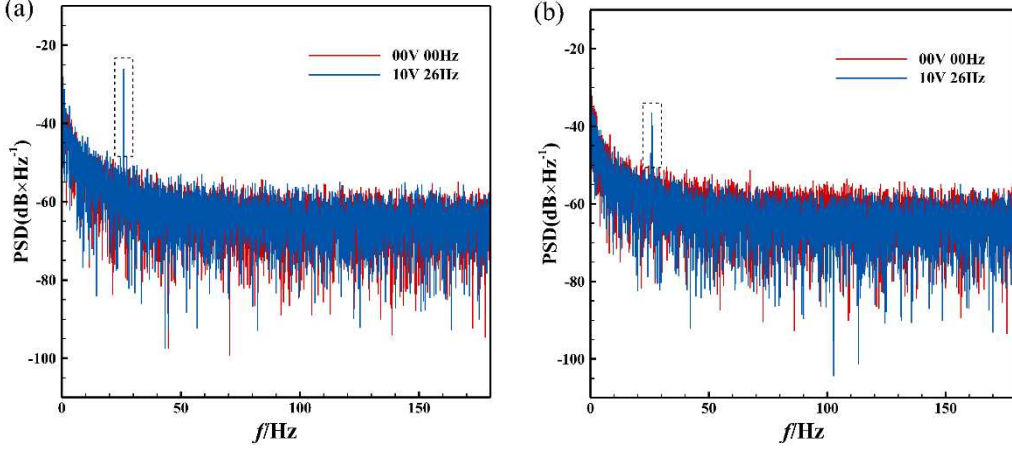


FIG. 6 PSD near the outlet calculated in (a) $x - y$ plane and (b) $x - z$ plane

PSD reflects the change of signal power with frequency in unit frequency, that is the distribution of signal power in frequency domain, which can be utilized to describe the intensity of noise. Fig.6(a) and 6(b) illustrate PSD at position $x/\delta_0 = 0$, $y/\delta_0 = 0.049$, $z/\delta_0 = 0$ in the streamwise-wall-normal plane and PSD at position $x/\delta_0 = 0$, $y/\delta_0 = 0.098$, $z/\delta_0 = 0$ in the streamwise-spanwise plane respectively. It can be seen from the two figures that the PSD curve of the flow field without control is relatively regular. However, under the action of the synthetic jet, a peak appears in PSD curve, marked by the rectangular dotted box. The frequency corresponding to the peak is 26Hz, which happens to be the excitation frequency of the synthetic jet, and the peak value represents the intensity of the disturbance.

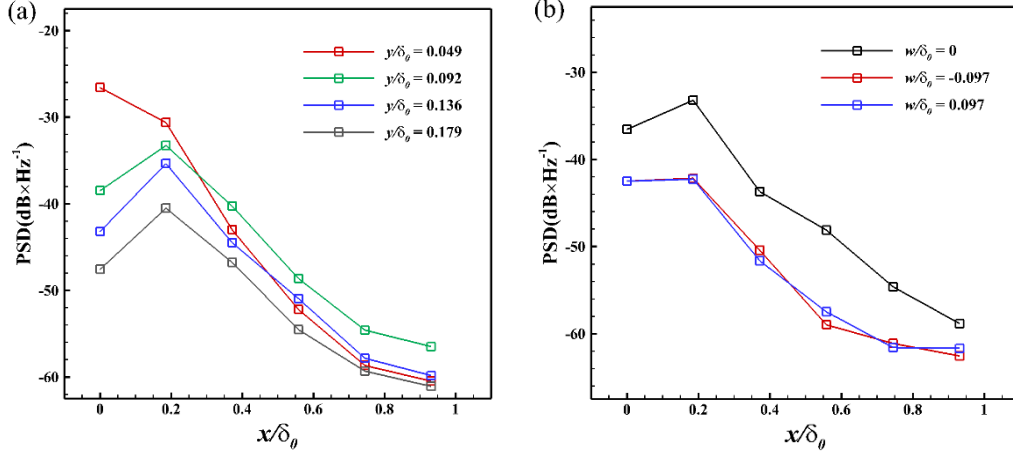


FIG. 7 Curves of PSD at different positions in (a) $x - y$ plane and (b) $x - z$ plane

By extracting PSD values at different locations with a frequency of 26Hz, the comparison of disturbance intensities at different locations can be obtained. Fig.7(a) shows the changes of PSD values at this frequency with the streamwise direction at different heights in the streamwise-wall-normal plane. It can be seen from the figure that the position ($x/\delta_0 = 0$, $y/\delta_0 = 0.049$) closest to the jet hole has the maximum disturbance intensity, which is most affected by the synthetic jet, and then decreases with the downstream. However, the curves at the other three heights all increased first and then gradually decreased, indicating that the maximum value of jet disturbance moved downstream at a higher position above the orifice. The reason is that the synthetic jet moves downstream due to momentum exchange under the influence of incoming flow velocity after it is ejected in y direction. The main disturbance area appears inclined at the exit position, which is consistent with the contour line of the difference of streamwise velocity showing an inclined ellipse. This also explains the faster decay of the curve downstream of the lowest height. In addition, the vicinity of the streamwise direction corresponding to the maximum value of the other three lines is also the place where the maximum velocity loss occurs in x direction. $y/\delta_0 = 0.092$, as the height of maximum disturbance when $x/\delta_0 > 0.3$ approximately, is also the height at which the speed deficit value decreases with x direction at the slowest rate (see Fig.5(a)). On the whole, when $x/\delta_0 < 0.3$, the disturbance intensity decreases gradually with y direction; when $x/\delta_0 > 0.3$, it increases first and then decreases with y direction. Fig.7(b) shows the changes of PSD values at a frequency

of 26hz with the streamwise direction at different spanwise positions in the streamwise-spanwise plane. As can be found from the figure, when $z/\delta_0 = 0$, namely, the middle position of the jet hole has a higher disturbance intensity than the two sides, which indicates that the influence of the synthetic jet decreases gradually on both sides. Besides, the disturbance intensity is symmetric along $z/\delta_0 = 0$. These are similar to the velocity deficit region shown in Fig.5(b). To sum up, there is a strong correlation between the perturbation intensity of the synthetic jet and the velocity deficit value, that is, where the perturbation intensity is larger, there is a more obvious velocity deficit.

3.2 Identification of vortex structures

The Lyapunov exponent measures the degree to which a system separates over time (iterations) due to small initial errors, and if it is greater than zero, it means that two particles with an infinitely small initial distance continue to move away at an exponentially increasing velocity. FTLE is not an instantaneous separation rate, but a measure of the average or composite separation between trajectories. In time-dependent flows, the instantaneous velocity field usually does not reveal the actual trajectory, that is, the instantaneous streamlines may deviate rapidly from the actual particle trajectory. However, FTLE is the combined effect of the flow because its calculation is based on particle trajectories, so it can better indicate the actual transmission behavior, and the individual problematic velocity fields does not significantly affect the results. Therefore, this method has good robustness. In the field of fluid mechanics, the Euler viewpoint proposes to observe the fluid at a fixed point in the domain at different time points, while the Lagrangian perspective is defined to study the flow field from the trajectory of the particle. FTLE is technically an Euler field, but is considered a Lagrangian quantity (Haller 2000). From the Lagrangian point of view, the boundary of the vortex structure separates the internal fluid from the ambient fluid. Due to the continuous rotation of the vortex structure, the two fluids near the two sides of the boundary will approach or move away in the next step, while its behavior speed is inversely proportional to the distance between the two fluids. At this time, the fluid particle near

the boundary has the maximum approaching or moving away velocity, and the corresponding Lyapunov exponent has a minimum or maximum value at this position. Subsequently, Haller (2001) proved through rigorous mathematical derivation that the extreme value of FTLE is the boundary of the vortex structure.

The transformation from the instantaneous velocity field to the trace field is the basic link of FTLE. The following bold fonts represent vectors. For any unsteady flow field $\mathbf{u}(\mathbf{x}, t) \in D$, the flow trace with initial position and time of \mathbf{x}_0 and t_0 , respectively, can be calculated as follows:

$$\begin{cases} \dot{\mathbf{x}}(t; t_0, \mathbf{x}_0) = \mathbf{u}(\mathbf{x}(t; t_0, \mathbf{x}_0), t) \\ \mathbf{x}(t_0; t_0, \mathbf{x}_0) = \mathbf{x}_0 \end{cases}.$$

In this case, we can define the flow map $\phi_{t_0}^t$ as the position map of a point in the domain moving from the initial time t_0 to the final time t , i.e.

$$\phi_{t_0}^t: D \rightarrow D: \mathbf{x}_0 \rightarrow \phi_{t_0}^t(\mathbf{x}_0) = \mathbf{x}(t; t_0, \mathbf{x}_0).$$

Then any point $\mathbf{x} \in D$ is located at $\phi_{t_0}^{t_0+T}(\mathbf{x})$ from t_0 . Assuming that there is a point \mathbf{y} infinitely close to \mathbf{x} at t_0 , it can be expressed as $\mathbf{x} + \delta\mathbf{x}(t_0)$, where $\delta\mathbf{x}(t_0)$ is an infinitesimal quantity. And over time, the distance between these two points will change, and the infinitesimal becomes:

$$\delta\mathbf{x}(t_0 + T) = \phi_{t_0}^{t_0+T}(\mathbf{y}) - \phi_{t_0}^{t_0+T}(\mathbf{x}) = \frac{d\phi_{t_0}^{t_0+T}(\mathbf{x})}{dx} \delta\mathbf{x}(t_0) + O(\|\delta\mathbf{x}(t_0)\|^2).$$

Its amplitude is

$$\|\delta\mathbf{x}(t_0 + T)\| = \sqrt{\langle \delta\mathbf{x}(t_0), \frac{d\phi_{t_0}^{t_0+T}(\mathbf{x})}{dx}^* \frac{d\phi_{t_0}^{t_0+T}(\mathbf{x})}{dx} \delta\mathbf{x}(t_0) \rangle},$$

where the symbol “*” represents the adjoint matrix. The symmetric matrix

$$\Delta = \frac{d\phi_{t_0}^{t_0+T}(\mathbf{x})}{dx}^* \frac{d\phi_{t_0}^{t_0+T}(\mathbf{x})}{dx}$$

is a finite-time version of the Cauchy-Green deformed tensor. If the definition:

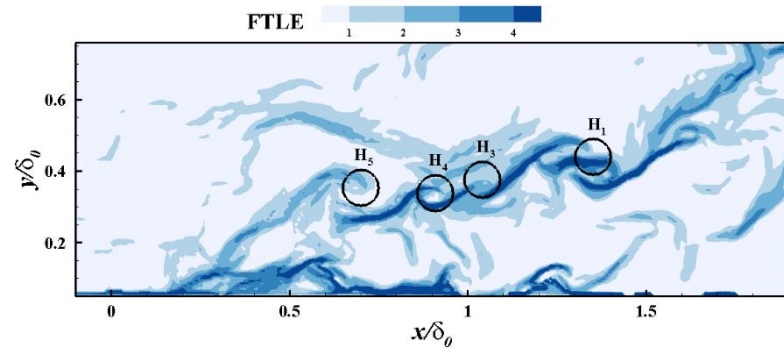
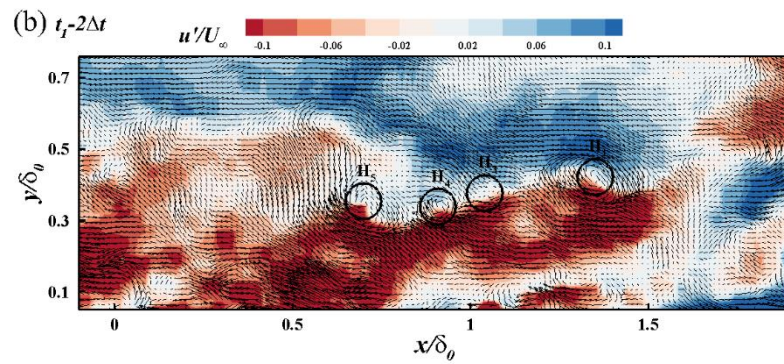
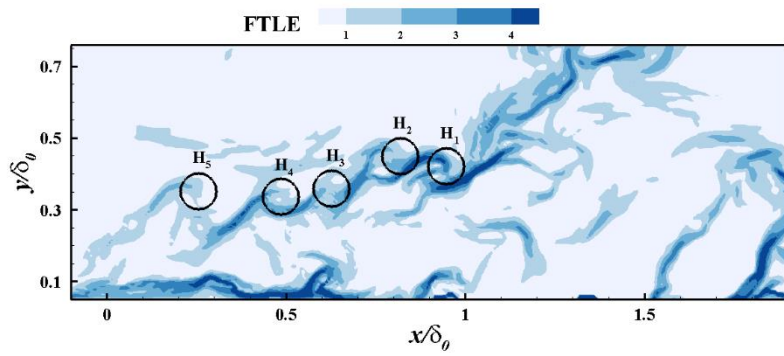
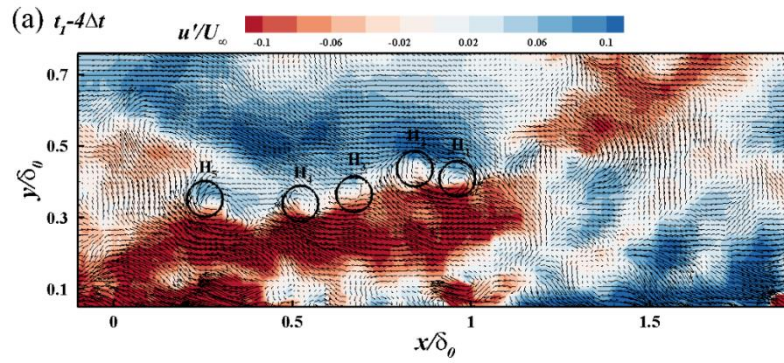
$$\sigma_{t_0}^T(\mathbf{x}) = \frac{1}{|T|} \ln \sqrt{\lambda_{\max}(\Delta)},$$

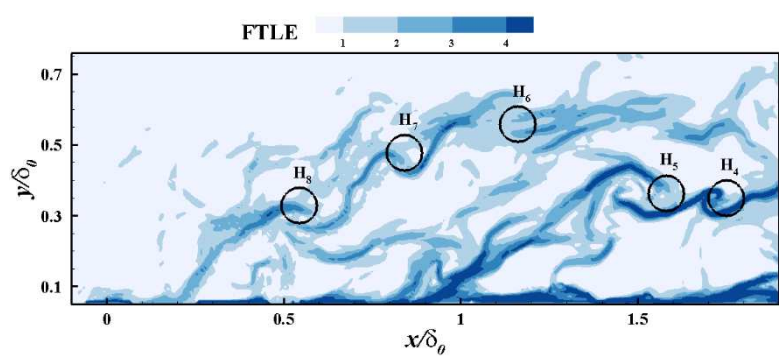
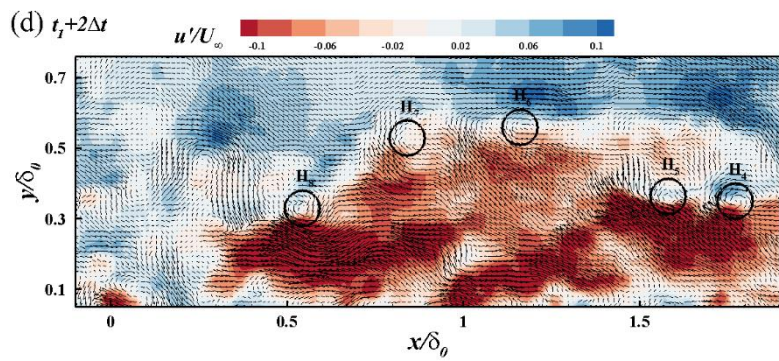
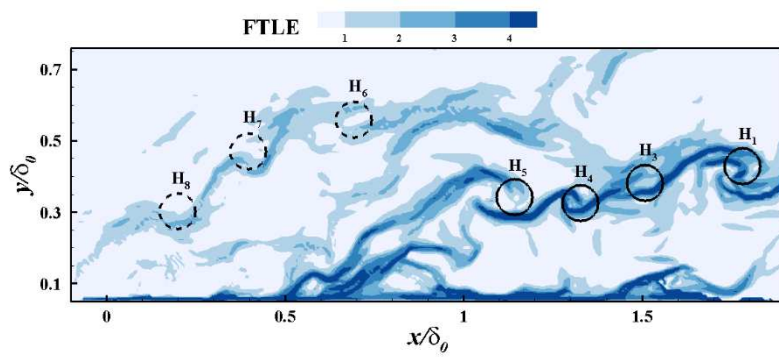
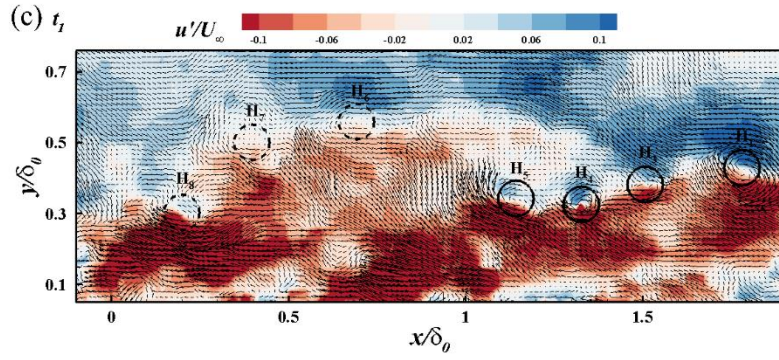
the maximum stretch rate occurs at:

$$\max_{\delta\mathbf{x}(t_0)} \|\delta\mathbf{x}(t_0 + T)\| = \sqrt{\lambda_{\max}(\Delta)} \|\delta\mathbf{x}(t_0)\| = e^{\sigma_{t_0}^T(\mathbf{x})|T|} \|\delta\mathbf{x}(t_0)\|.$$

At this time, $\sigma_{t_0}^T(\mathbf{x})$ is the Lyapunov exponent of the point $\mathbf{x} \in D$ at t_0 after the

finite integration time T .





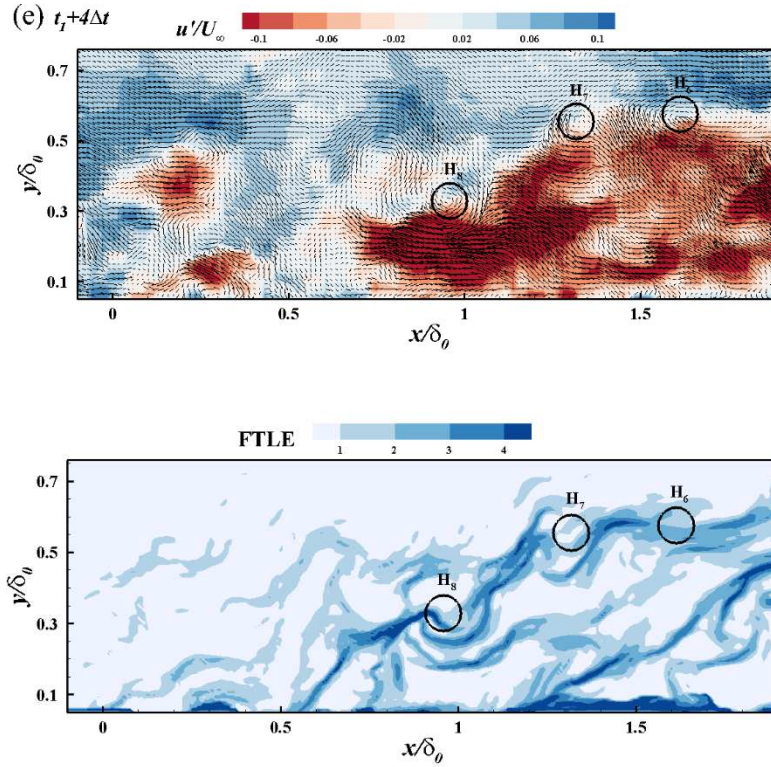


FIG. 8 The contours of hairpin vortex structures on smooth flat wall without control at the reference time of (a) $t_1 - 4\Delta t$, (b) $t_1 - 2\Delta t$, (c) t_1 , (d) $t_1 + 2\Delta t$, (e) $t_1 + 4\Delta t$

Based on the data measured in this experiment without control, the hairpin vortex packet structure and the generation process of the new hairpin vortex are successfully captured. Under the shooting conditions of this time, three formed hairpin vortex packets are found in about 2000 continuous velocity fields, and a representative one will be selected for display below. Fig.8 depicts the FTLE contours of a smooth plate without control at different times, and for comparison, the fluctuation velocity contours and vector field at the same time are added. Time t_1 is defined as the moment when the new hairpin vortices are about to be generated, and the time interval Δt is set to 0.05s. From each instantaneous field, it can be found that the black solid circles mark the clockwise vortex region, and these regions are considered to be the vortex heads of the hairpin vortices. In the corresponding FTLE field, which is also marked with black circles at the same position, it can be seen that this region appears at the upper right of each helical structure. According to the FTLE derivation, these helical structures are the vortex legs of the hairpin vortices. However, the identifications of the hairpin head by the instantaneous fields and the FTLE fields are not completely consistent, which

may be explained by a small error between the instantaneous quantities and integral quantities.

At time $t_1 - 4\Delta t$ (Fig.8(a)), it can be found that five hairpin vortices (from H_1 to H_5) appear upstream of FOV, aligning with the free flow at a certain angle to form a hairpin vortex packet. And it can be seen that a large-scale low-momentum region is generated inside the hairpin vortex, while the outside is a high-speed fluid region, which is consistent with the findings of Adrian et al. (2000). These two regions are thought to be generated under the synergistic induction of hairpin vortices. At time $t_1 - 2\Delta t$ (Fig.8(b)), the vortex core of H_2 on the downstream side is slightly higher than of H_1 , and thus it has a slightly larger streamwise velocity, so that the vortex head of H_2 gradually approaches H_1 and the vortex legs are elongated due to the speed difference caused by the height. The two vortices tend to merge. The hairpin vortex packet model explains the phenomenon of multiple ejections of fluid in a turbulent burst (Alfredsson and Johansson 1984). At time t_1 (Fig.8(c)), induced by the hairpin vortex packet, a strong ejection event is generated upstream of H_5 , which subsequently causes the low-velocity fluid below it to jet into the upper region and shear with the high-velocity fluid at a higher position. The new hairpin vortex begins to gradually form under the action of shear force, which is marked with a black dashed circle. Meantime, it is shown in the FTLE field that the vortex heads of the two vortices in the fusion state are basically in the same streamwise direction, but only one vortex can be seen in the instantaneous field, indicating that the two vortices have been fused, and H_1 is used to mark the vortex after fusion. At the time $t_1 + 2\Delta t$ and $t_1 + 4\Delta t$ (Fig.8(d) and 8(c)), a new hairpin vortex packet consisting of three hairpin vortices H_6 , H_7 and H_8 is revealed and develops downstream over time. During the whole time period, the large-scale low-momentum region plays a crucial role in the generation and development of the hairpin vortex packet. According to the Taylor's frozen hypothesis, it can be concluded that the streamwise scale of this region is about $2\delta_0$.

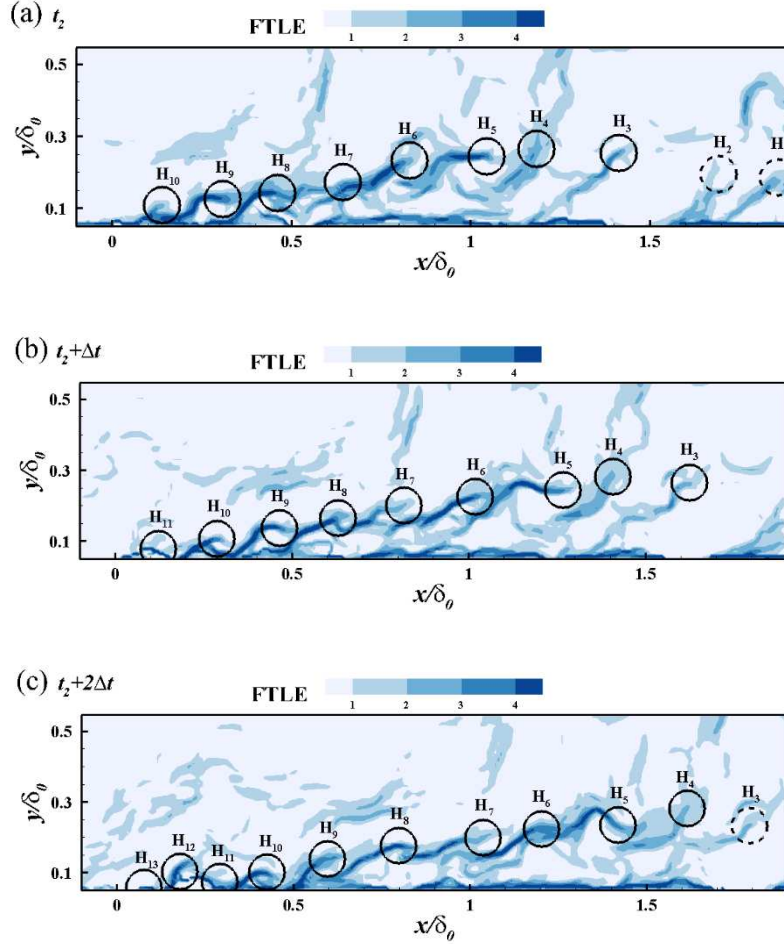


FIG. 9 The contours of the hairpin vortices generated under the control of the synthetic jet at the reference time of (a) t_2 , (b) $t_2 + \Delta t$, (c) $t_2 + 2\Delta t$

Berk and Ganapathisubramani (2000) experimentally found that the applied periodic synthetic jet can generate vortex structures periodically. Fig.9 illustrates the FTLE fields with the flow field under the synthetic jet control at different times. t_2 is the time randomly selected in the continuous field sequence. At time t_2 (Fig.9(a)), it can be seen that there are eight formed hairpin vortices (from H_3 to H_{10}) arranged in a row, and two hairpin vortices (H_1 and H_2) that gradually dissipate, which is consistent with what Chaudhry and Zhong (2014) observed with the flow display. These ordered hairpin vortices are periodically generated by the synthetic jet, while the earlier hairpin vortices are located further downstream due to the streamwise velocity. They are arranged obliquely, which indicates that their development trend is similar to that of hairpin vortices on smooth plates. The curve formed by each vortex core is almost close to zero contour line in Fig.5(a), which indicates that the large-scale low-

momentum region is caused by the joint induction of hairpin vortices. Meanwhile, the generation of the low-speed streak in Fig.5(b) is also explained, and zero contour line in the figure can roughly describe the motion trend of the two hairpin vortex legs. At time $t_2 + \Delta t$ and $t_2 + 2\Delta t$ (Fig.9(b) and 9(c)), new hairpin vortices (from H_{11} to H_{13}) keep appearing, while old hairpin vortices (H_3) gradually disappear. However, from the comparison between Fig.9(a) and Fig.9(c), it can be found that the position where the hairpin vortex dissipates is not certain, which shows that the disturbance of the synthetic jet gradually decreases with the downstream, so that the hairpin vortex located at a more downstream position is more susceptible to the instability of the incoming flow.

3.3 Dynamic contributions of wall friction resistance coefficient

Passive controls such as grooves and superhydrophobicity can uniformly affect the flow field, while the disturbance generated by the synthetic jet is non-uniform and local, so the drag reduction rate it produces will also change with different position.

For a full-developed TBL, the local wall frictional drag coefficient c_f can be decomposed into four different dynamic contributions: the boundary layer thickness contribution c^δ , the Reynold shear stress term c^T , the mean convection term c^C , and the spatial development term c^D . The formula (FIK identity) can be expressed in the following form:

$$c_f(x) = c^\delta(x) + c^T(x) + c^C(x) + c^D(x) = \frac{4(1-\delta^*)}{Re_\delta} + 2 \int_0^1 2(1-y) (-\overline{u'v'}) dy + 2 \int_0^1 2(1-y) (-\overline{uv}) dy - 2 \int_0^1 (1-y)^2 \left(\frac{\partial \overline{uu}}{\partial x} + \frac{\partial \overline{u'u'}}{\partial x} - \frac{1}{Re} \frac{\partial^2 \overline{u}}{\partial x^2} \right) dy,$$

where δ^* represents the displacement thickness. In the calculation process, all parameters in the formula are dimensionless with the outer scale length $\delta_0 = 0.046\text{m}$ and outer scale velocity $U_\infty = 0.255\text{m/s}$. It should be noted, however, that c^C and c^D are not present in fully developed channel flow and pipe flow.

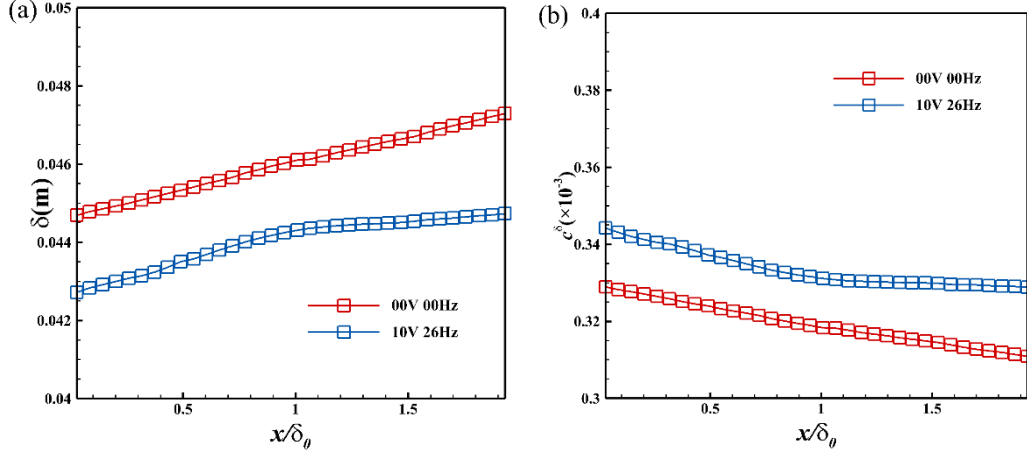


FIG. 10 The curves of (a) nominal boundary layer thickness and (b) c^δ with x direction

In the above formula, the Reynolds number $Re_\delta = \frac{U_\infty \delta}{\nu}$, and the nominal boundary layer thickness δ is based on the normal height corresponding to $0.99U_\infty$. Fig.10 demonstrates the curves of nominal boundary layer thickness δ and its contribution c^δ with the streamwise direction, respectively. It can be observed from Fig.10(a) that in the uncontrolled smooth plate, the thickness of the developing TBL is gradually increased and its increment remains basically constant within the same displacement. Under the periodic perturbation of the synthetic jet, the thickness of the boundary layer at any streamwise direction position is obviously thinned. After applying control, the curve shows a trend of faster growth when $x/\delta_0 < 1$ and slower growth when $x/\delta_0 > 1$ approximately. Sano and Hirayama (1985) found that the synthetic is essentially periodic blowing and sucking, and for the same mass flux, the average effect in the flow field is vertical upward blowing. The resulting normal velocity will cause the low-speed fluid downstream of the jet hole to move upward, resulting in a large bulge in the boundary layer thickness curve (blue curve), which is consistent with the conclusion obtained by Kim and Adrian (1999). In the curves of Fig.10(b), the values of c^δ with control are all larger than those without control, indicating that the synthetic jet makes the boundary layer thickness become a drag-increasing term.

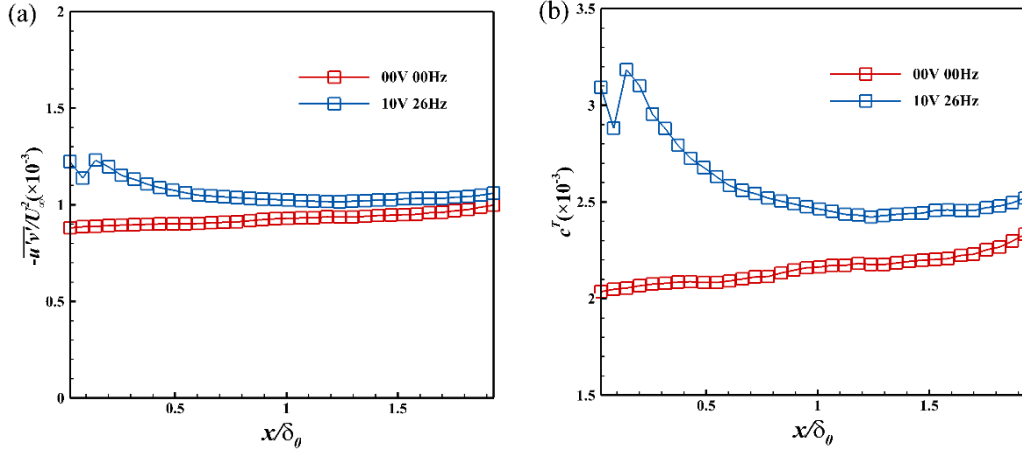


FIG. 11 The curves of (a) Reynolds shear stress and (b) c^T with x direction

The value range of y is the area between the upper surface of plate and the height corresponding to the thickness of TBL. Fig.11(a) shows the control curve and uncontrolled curve of the mean value of Reynolds shear stress in the boundary layer with the streamwise direction. As can be seen from the figure, the large range disturbance of the synthetic jet increases the Reynolds shear stress in the whole region. In the vicinity of the jet hole, the curve decreases first, then increases and then slowly decreases, resulting in a local maximum value, while the maximum velocity deficit occurs just near the corresponding streamwise direction position in Fig.5(a). When there is no control, the Reynolds shear stress shows a trend of slowly increasing with the streamwise direction. It can be considered that the continuous development of TBL makes the coherent structure in the flow field more and more complex and disorderly, which is consistent with the curve trend obtained by Kametani and Fukagata (2011). It is observed from the difference between the two curves that the gap becomes smaller and smaller along the downstream, which is caused by the continuous attenuation of disturbance and the gradual separation of the flow field from the influence of the synthetic jet, and this is consistent with the description in Fig.7(a). Fig.11(b) depicts the curves of the Reynold shear stress term c^T with the streamwise direction in two cases. It can be seen that the variation trend of c^T is similar to that of Reynolds shear stress, and it also indicates that the Reynolds shear stress term increases the wall friction coefficient under the action of the synthetic jet, which is a drag increasing term.

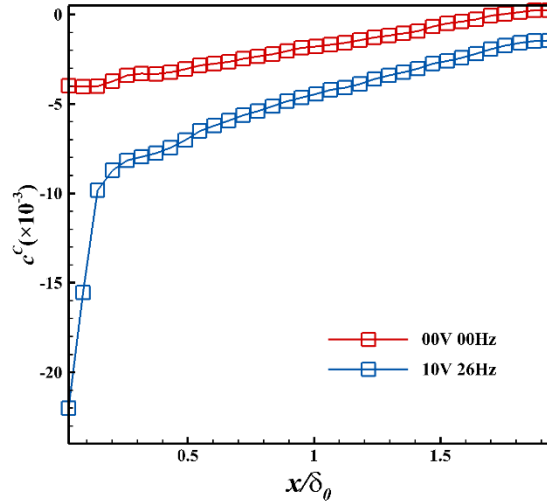


FIG. 12 The curves of c^C with x direction

Fig.12 illustrates the curves of mean convection term c^C with the streamwise direction under controlled and uncontrolled conditions. It can be seen that the average convection term has a negative contribution to the wall frictional drag coefficient in both cases, and its contribution gradually decreases with the downstream. In the region close to the jet hole, the synthetic jet makes the mean convective term more intense, but it also decays faster downstream, and finally maintains a similar decay rate with the uncontrolled case.

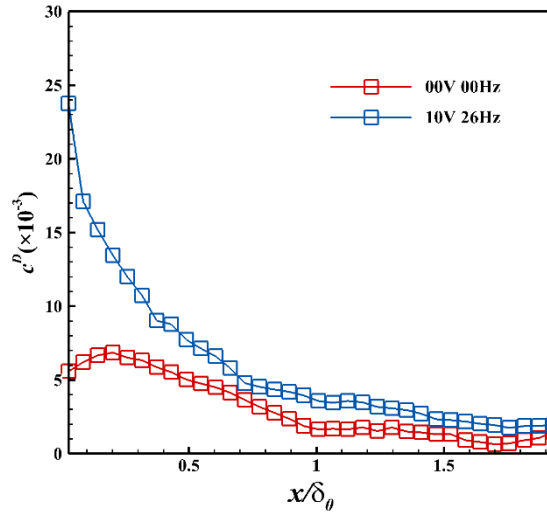


FIG. 13 The curves of c^D with x direction

Fig.13 demonstrates the curves of the spatial development term c^D with the streamwise direction in two cases. It can be found that both curves are positive, representing the incremental drag term. The synthetic jet makes the spatial development term have a similar trend with the mean convective term, which is more intense near

the hole, as the downstream curve gradually approaches the undisturbed condition.

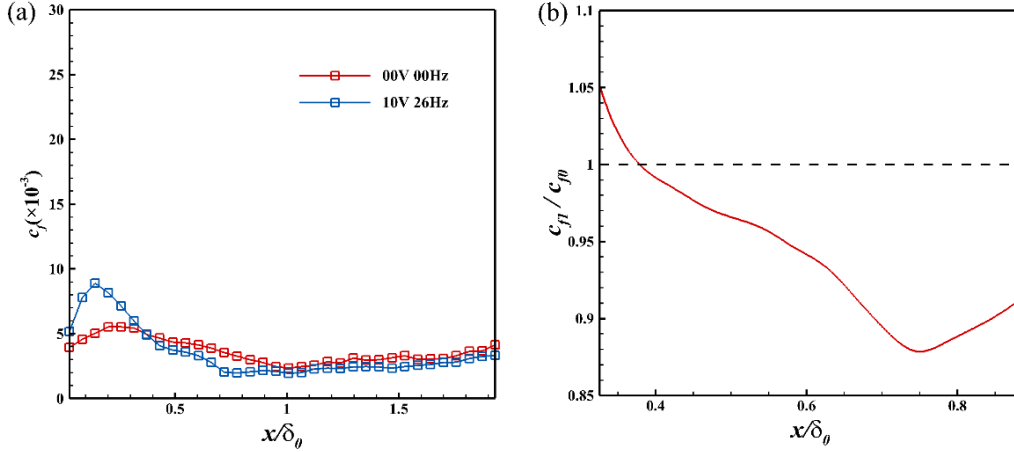


FIG. 14 The curves of (a) c_f and (b) the skin-friction drag coefficient ratio with x direction

Finally, according to the FIK identity, the four dynamic contributions are added together to obtain the curve of local wall friction drag coefficient c_f with the streamwise direction, as depicted in Fig.14(a). It can be seen from the figure that the two curves generate an intersection point at the streamwise direction position of about $0.38\delta_0$. On the left side of the intersection point, the synthetic jet shows drag increase, while on the right side, it shows drag reduction. As the two curves keep approaching downstream, it shows that the drag reduction effect is gradually weakened, which also reflects that the drag reduction effect produced by the synthetic jet is local. Fig.14(b) describes the curve of the ratio of wall friction drag coefficients with and without control with the streamwise direction, calculated using small FOV data processed by the SPEC algorithm. When $c_{f1}/c_{f0} > 1$, the result is drag increase, on the contrary, drag reduction, and the smaller value is, the better the drag reduction effect. In Fig.14(b), the streamwise direction position corresponding to the critical point of drag increase and decrease is basically the same as that in Fig.14(b). At about $x = 0.75\delta_0$, the drag reduction rate reaches a maximum of 12.2%, and gradually decreases due to the disturbance of the synthetic jet as the downstream continues to weaken. Although the drag reduction effect shown in the two figures is similar, there is a certain difference in drag reduction intensity, which may be caused by the fact that the average pressure gradient made by the synthetic jet is non-zero, while the average pressure gradient is assumed to be zero in the derivation of FIK identity. Therefore, FIK identity is more

suitable to study the drag reduction mechanism of the synthetic qualitatively.

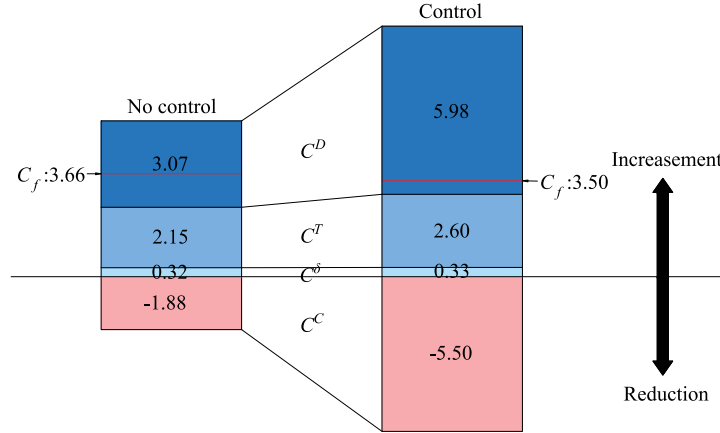


FIG. 15 The dynamic contributions to the overall wall friction resistance coefficient ($\times 10^{-3}$)

In the FIK identity, some terms show positive contribution to frictional resistance, while others show negative contribution. In the fully developed smooth plate flow field, the boundary layer thickness term, Reynolds stress term and spatial development term are used to increase the wall friction resistance, and the mean convection term is used to reduce it. After the synthetic jet control, all the components increased, but still retained their original effects. It can also be found from the comparison of the above curves that, in the downstream of the jet hole, the mean convection term c^C is strong resistance reduction factor, and the spatial development term c^D is the strong resistance enhancement factor. From these analyses, we can conclude that the mean convection term c^C , including $\bar{u}\bar{v}$, plays a very important role in determining the drag reduction or increase of the synthetic jet. If the average convection term can be enhanced and the fluctuation of spatial development term can be controlled, better drag reduction effect will be achieved. This conclusion can also be explained more clearly by the decomposition of the overall friction coefficient C_f , which is expressed as follows:

$$C_f = \frac{1}{L_{ctr}} \int_0^{L_{ctr}} c_f dx = \frac{1}{L_{ctr}} \int_0^{L_{ctr}} c^\delta dx + \frac{1}{L_{ctr}} \int_0^{L_{ctr}} c^T dx + \frac{1}{L_{ctr}} \int_0^{L_{ctr}} c^C dx + \frac{1}{L_{ctr}} \int_0^{L_{ctr}} c^D dx = C^\delta + C^T + C^C + C^D.$$

In the formula, L_{ctr} is the streamwise direction range calculated. The results are shown in Fig.15. In the area from the jet hole ($x = 0$) to $x = 1.93\delta_0$, the synthetic jet

reduces the friction resistance coefficient from 3.66 to 3.50, achieving the overall drag reduction effect. The increment of negative contribution of the average convection term c^C is larger than that of the total positive contribution of the other three terms, which plays a key role in drag reduction.

3.4 Proper orthogonal decomposition

The complexity of TBL flows mainly comes from the coherent structures contained therein. As Liepmann (1979) said, the most important aspect of coherent structures in turbulence is to control turbulence by controlling such structures. Q2 event and Q4 event, as coherent structures, are the main sources of Reynolds shear stress and turbulent kinetic energy (TKE) in the near-wall region. Especially the Q4 event is also one of the reasons for the increase of skin friction resistance (Xu et al. 2013).

The coherent structure in TBL has the characteristics of multi-scale. In this part, the flow field is divided into different scales according to the energy content by using POD. Bakewell and Lumley (1967) first applied POD to the field of turbulence and extracted the large-scale structure in the near-wall region of a circular pipe flow. Then Sirovich et al. (1990) utilized digital imaging analysis to give the specific implementation means of POD, and proposed that the sum of the first several terms obtained by decomposition can represent the large-scale structure, while the rest represent the small-scale structure. The specific process of POD is as follows:

Firstly, the fluctuation velocity field matrix should be constructed. For discrete data, it can be written as

$$U = \begin{bmatrix} U'_{11} & U'_{12} & \cdots & U'_{1N} \\ U'_{21} & U'_{22} & \cdots & U'_{2N} \\ \vdots & \vdots & \ddots & \vdots \\ U'_{M1} & U'_{M2} & \cdots & U'_{MN} \end{bmatrix} = [U'(t_1) \quad U'(t_2) \quad \cdots \quad U'(t_N)].$$

In the above equation, the wall-normal and streamwise fluctuation velocities are collectively described as $U' = (u', v')$, while M and N represent the number of space points and time points respectively. Then, singular value decomposition (SVD) is utilized to express U as

$$U = L\Sigma R^T,$$

where, Σ is the singular value matrix, L and R are the left and right eigenvectors of singular values respectively. In this case, the correlation function matrix of the velocity field is

$$C = U^T U = R \Sigma L^T L \Sigma R^T = R \Lambda R^T.$$

In the formula, Λ represents the eigenvalue matrix of C , and R is the corresponding eigenvector. The elements in the eigenvalue matrix Λ are arranged in descending order, and the corresponding eigenvectors R are also arranged in the order of Λ . The i th eigenvalue is the contribution of the i th mode to the total TKE of the flow field, which is shown in a proportional form:

$$E_i = \Lambda_i / \sum_{i=1}^N \Lambda_i.$$

At this point, the fluctuation velocity field can be expressed as:

$$U(t_n) = \sum_{i=1}^N a_i(t_n) \Phi_i,$$

where, the basis function $\Phi_i = \frac{UR_i}{\|UR_i\|}$, and the time coefficient $a_i(t_n) = \Phi_i^T U(t_n)$.

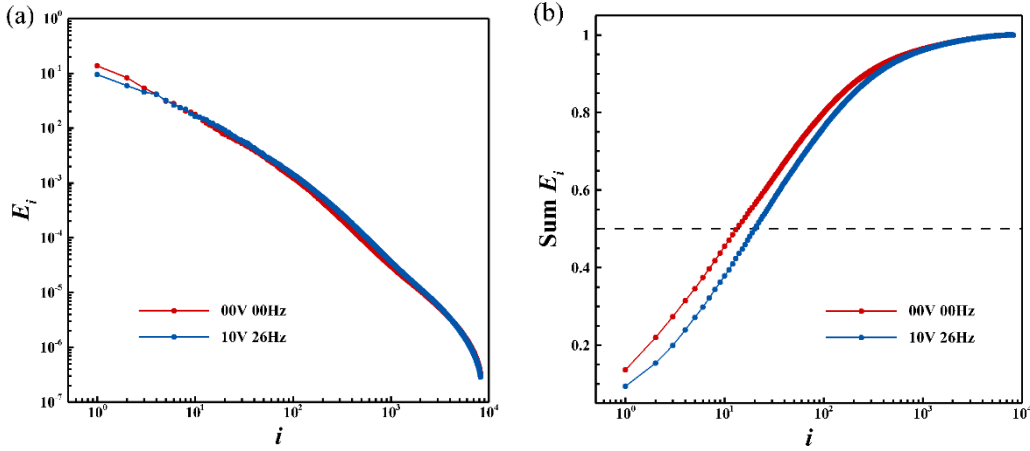


FIG. 16 The curves of POD energy contribution: (a) contribution of single mode, (b) cumulative contribution of modes

Generally speaking, large-scale structure has higher energy content, while small-scale structure has lower energy content. Here, continuous 8000 instantaneous fluctuation velocity fields are applied to POD. Fig.16(a) illustrates the curves of the TKE of a single mode with and without control with respect to the number N of modes. In Fig.16(a), since the POD method arranges the modes according to their energy contributions, the first mode always has the highest energy and the energy is decreasing. Under the condition of control, the energy contribution of the first three modes

decreases obviously, and the contribution of the other high order modes increases slightly, indicating that the synthetic jet weakens the large-scale energetic structure while strengthens the small-scale energetic structure. POD can not only separate the coherent structures at different scales in turbulent flow according to the energy contribution, but also reconstruct the low-dimensional dynamical system based on the scale separation. Fig.16(b) shows the ratio of the accumulated energy (Sum $E_i = \sum_{m=1}^i E_m$) of the first i modes to the overall TKE. It can be seen from the figure that the accumulated energy of any mode after disturbance is almost smaller than that without disturbance, which indicates that the weakening effect of the synthetic jet on large-scale structure is strong. At this point, the lower-order POD modes with higher energy reconstruct the large-scale flow field, while the remaining POD modes constitute the small-scale flow field. However, the selection of the boundary between large and small scales is subjective. This part refers to the views of Wu and Christensen (2010), and selects 50% of accumulative energy as the threshold value. With and without control, the number of modes corresponding to 50% of the accumulated energy is 20 and 13, respectively.

In order to explore the change of large-scale and small-scale bursting events after applying the synthetic jet, we extract them from the reconstructed two scale flow fields using an improved quadrant splitting method (IQSM) (Guan et al. 2013; Yang and Jiang 2012). Firstly, the structure function of two-dimensional local average velocity based on discrete data needs to be given:

$$\begin{aligned}\delta u_x(x_0, l_x; y_0) &= \overline{u(x, y_0)}_{x \in [x_0, x_0 + l_x]} - \overline{u(x, y_0)}_{x \in [x_0 - l_x, x_0]} \\ \delta v_y(x_0; y_0, l_y) &= \overline{v(x_0, y)}_{y \in [y_0, y_0 + l_y]} - \overline{v(x_0, y)}_{y \in [y_0 - l_y, y_0]},\end{aligned}$$

where $l_{x,y} = 4$ is the detection range of the detection point in four directions. In the physical sense, this function represents the compression or stretching of the turbulent local structures in the direction of study. In this case, IQSM formula can be expressed as

$$D(x_0, l_x; y_0, l_y) =$$

$$\left\{ \begin{array}{ll} 1(Q2) & \text{if } \begin{array}{l} u' < 0 \text{ and } \delta u_x^- < 0 \text{ and } \delta u_x^+ > 0 \text{ and} \\ v' > 0 \text{ and } \delta v_y^- > 0 \text{ and } \delta v_y^+ < 0 \end{array} \\ -1(Q4) & \text{if } \begin{array}{l} u' > 0 \text{ and } \delta u_x^- > 0 \text{ and } \delta u_x^+ < 0 \text{ and} \\ v' < 0 \text{ and } \delta v_y^- < 0 \text{ and } \delta v_y^+ > 0 \end{array} \\ 0 & \text{otherwise} \end{array} \right.$$

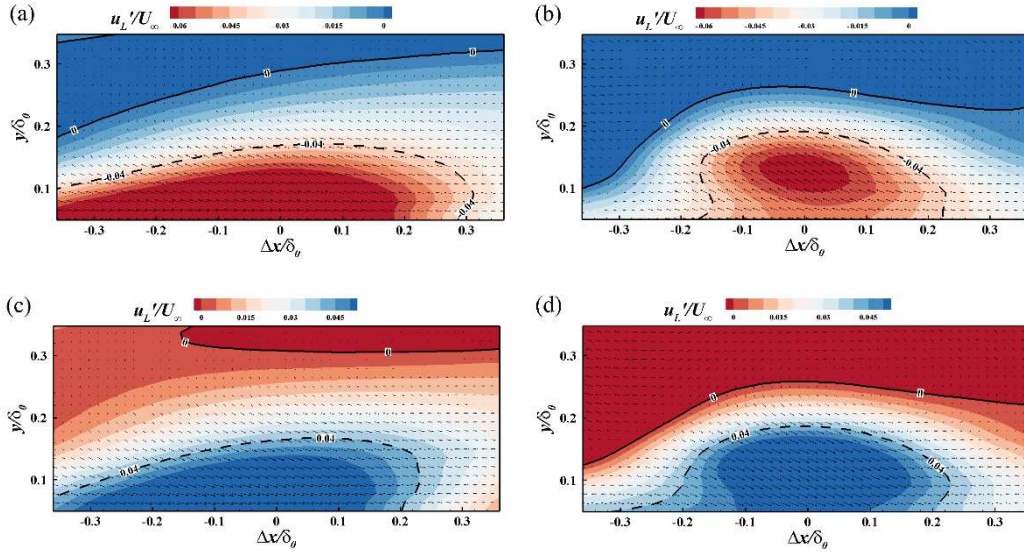


FIG. 17 Vectors of fluctuation velocity and the streamwise velocity contours of large-scale structure: (a) Q2 event without control, (b) Q2 event with control, (c) Q4 event without control, (d) Q4 event with control at $y/\delta_0 = 0.12$

According to IQSM, the detected points are the locations with the strongest local burst events, and the surrounding areas can be extracted. The universal burst events in the flow field can be characterized by superposition and average of these areas (conditional average). The detection region without control is the whole flow field, while in the controlled case, it is the range of $x/\delta_0 > 0.25$, for the sake of studying the drag reduction mechanism. In both cases, the near-wall region with normal height $y/\delta_0 = 0.12$ is selected. After the conditional averaging technique, the position of the checkpoint is defined as $\Delta x/\delta_0 = 0$, $y/\delta_0 = 0.12$.

Fig.17 depicts the fluctuation velocity vectors and streamwise velocity contours for large-scale Q2 and Q4 events under the two conditions. The zero isoline is marked by solid black line, and the dashed black line is the area of $u'_L/U_\infty = 0.04$. It can be seen from Fig.17(a) and 17(b) that the narrowing trend of the range of zero isolines represents that the influence range of large-scale Q2 events on local areas becomes smaller after control. The dimensionless streamwise length of $u'_L/U_\infty = 0.04$ is about 0.7 without control and 0.4 with control, which indicates that the synthetic jet reduces

the scale of large-scale Q2 events, but the intensity at the center is not significantly weakened. These similar phenomena are observed in the large-scale Q4 events shown in Fig.17(c) and 17(d). In the picture, normal uplift occurs on the contour line $u'_L/U_\infty = 0.04$ under controlled condition, denoting that the synthetic jet drives large-scale structures away from the wall, so as to reduce the normal transport of energy and momentum on the wall, and weaken the high friction resistance caused by the high-speed fluid sweep in near-wall region. The bursting events are mainly induced by streamwise vortices, so the results indirectly prove that the uplift effect of the synthetic jet raises the normal height of large-scale streamwise vortices, which is consistent with the findings of Lu et al.²³.

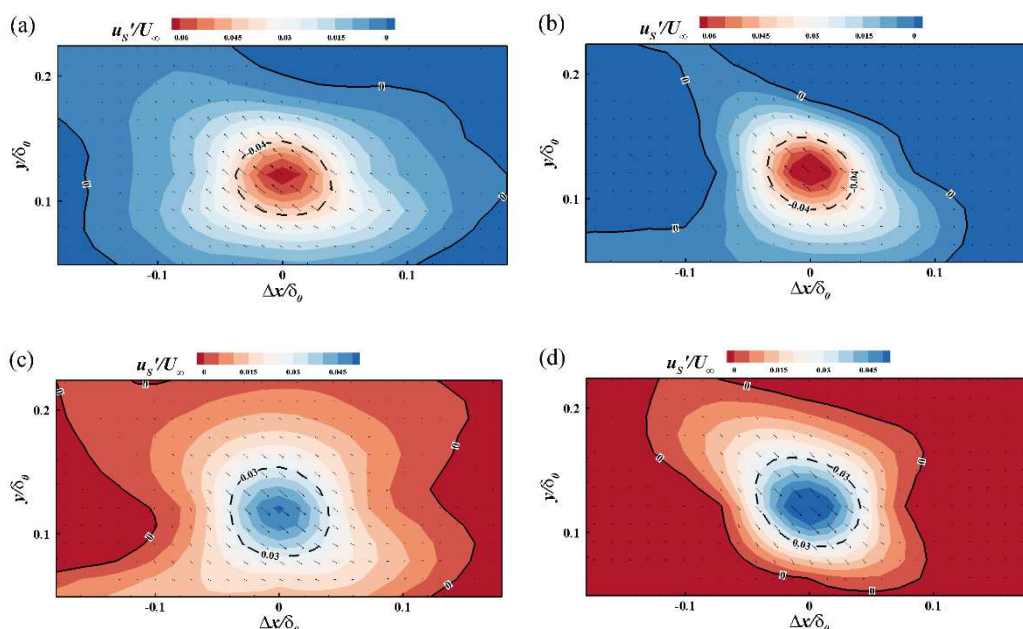


FIG. 18 Vectors of fluctuation velocity and the streamwise velocity contours of small-scale structure: (a) Q2 event without control, (b) Q2 event with control, (c) Q4 event without control, (d) Q4 event with control

Fig.18 describes the fluctuation velocity vectors and streamwise velocity contours for small-scale Q2 and Q4 events under the two conditions. Black solid line is zero contour line. After the control is applied, the black dashed line shows the area with a similar range to the previous one. It can be found from these figures that both the streamwise scale and the normal scale of the zero isoline are obviously reduced, which indicates that the synthetic jet limits the scope of small-scale bursting events in the near-wall region of the flow field. Within the dashed line, the synthetic jet increases the

intensity of small-scale events, which is also responsible for the increased energy contribution of the POD higher-order modes, but its intensity decays more rapidly with distance.

In conclusion, the influence range of large-scale and small-scale bursting events is reduced after applying the synthetic jet. The normal transport of energy and momentum brought to the wall by large-scale Q2 events is weakened, and the friction resistance caused by large-scale Q4 events is reduced. Therefore, the drag reduction effect is obtained in the downstream of the jet hole.

4 Conclusion

The instantaneous velocity fields of the $x - y$ plane and $x - z$ plane were collected by a 2D TR-PIV system. The average velocity profile in the near wall region calculated by the SPEC algorithm is fitted with linear law to obtain the wall friction resistance, and the results exhibit that under the action of synthetic jet, and average drag reduction rate is 6.2% in the range of $0.33\delta_0 \sim 0.88\delta_0$ downstream of the jet hole.

The difference between the controlled and uncontrolled average velocities shows that the synthetic jet generates a wide range of momentum deficit downstream and its height increases with the streamwise direction. A low-speed streak is formed, and its spanwise range expands to both sides along x direction. When the sinusoidal synthetic jet with a fixed frequency of 26Hz is applied, the PSD corresponding to 26Hz can represent the disturbance intensity of the jet. The results show that the disturbance is inclined under the influence of incoming flow, and it is accompanied by a large velocity deficit where the disturbance is strong.

The coherent structures in instantaneous flow field are visualized by FTLE technique. A hairpin vortex packet composed of five hairpin vortices is captured in a smooth plate without control, and a large-scale low-speed region is induced beneath it. A strong Q2 event exists in the upstream of the vortex packet, which raises the low-velocity fluid below and shear with the high-velocity fluid at a higher position, resulting in the generation of new hairpin vortices. In controlled circumstances, it can be found

that the hairpin vortices are continuously generated near the jet opening under the influence of periodic disturbance of the synthetic jet. The evolution of these hairpin vortices just coincides with the variation trend of the velocity deficit region and the low-speed streak shown in Fig.5. It indicates that the low-speed region is caused by the joint induction of these hairpin vortex heads, and the generation of low-velocity streak is related to the two forward vortices (vortex legs).

The drag reduction mechanism of synthetic jet is investigated qualitatively using FIK identity. The results exhibit that c^δ , c^T , c^C and c^D are enhanced to varying degrees under control, while the mean convection term c^C and the spatial development term c^D , as strong drag reduction factor and strong drag enhancement factor respectively, play a crucial role in drag reduction due to the regulation of the synthetic jet. Meantime, it is verified that the drag reduction effect is local. According to the wall friction coefficient calculated based on the SPEC algorithm, it can be seen that the synthetic has a drag reduction effect when $x/\delta_0 > 0.38$. The drag reduction rate reaches the maximum at about $x/\delta_0 = 0.75$, which is 12.2%, and then its strength gradually decreases with the downstream.

After using POD, it is acquired that the synthetic jet weakens the energy proportion of the large-scale energetic structure in low-order modes, but enhances the small-scale energy proportion. The large-scale flow field is reconstructed according to 50% of the accumulated energy of each mode flow field obtained by POD, and the remaining modes are composed of small-scale flow field. The conditional average is utilized to extract the bursting events at the height of $y/\delta_0 = 0.12$. The results show that in the region $x/\delta_0 > 0.25$, the synthetic jet reduces the influence range of large-scale and small-scale bursting events, and weakens the normal transport of momentum and energy in the near wall region caused by large-scale Q2 events and the wall friction resistance caused by large scale Q4 events, so that the drag reduction effect is achieved.

Acknowledgments

This work is supported by the National Natural Science Foundation of China (Grant No. 11732010, 11972251, 11872272, 11902218, 12172242), Chinesisch-Deutsche Zentrum für Wissenschaftsförderung [grant number GZ1575] and the Ministry of Industry and Information Technology (Grand No. [2019] 360)

Declarations

1 Ethical Approval

Not applicable.

2 Competing interests

All authors certify that they have no affiliations with or involvement in any organization or entity with any financial interest or non-financial interest or competing interest in the subject matter or materials discussed in this manuscript.

3 Authors' contributions

Jinhao Zhang wrote the main manuscript text and conducted experiments .Biaohui Li helped with the experiment and Nan Jiang provided experimental materials and examination of the article. All authors provided suggestions for revision of the manuscript.

4 Funding

This work is supported by the National Natural Science Foundation of China (Grant No. 11732010, 11972251, 11872272, 11902218, 12172242), Chinesisch-Deutsche Zentrum für Wissenschaftsförderung [grant number GZ1575] and the Ministry of Industry and Information Technology (Grand No. [2019] 360)

5 Availability of data and materials

The data that support the findings of this study are available from the corresponding author upon reasonable request.

References

- Acarlar MS, Smith CR (1987) A study of hairpin vortices in a laminar boundary layer. Part 1. Hairpin vortices generated by a hemisphere protuberance. *J Fluid Mech* 175:1-41. Doi: <https://doi.org/10.1017/S0022112087000272>
- Acarlar MS, Smith CR (1987) A study of hairpin vortices in a laminar boundary layer.

- Part 2. Hairpin vortices generated by fluid injection. *J Fluid Mech* 175:43-83. Doi: <https://doi.org/10.1017/S0022112087000272>
- Adrian RJ, Meinhardt CD, Tomkins CD (2000) Vortex organization in the outer region of the turbulent boundary layer. *J Fluid Mech* 422:1-54. Doi: <https://doi.org/10.1017/S0022112000001580>
- Alfredsson PH, Johansson AV (1984) Time scales in turbulent channel flow. *Phys Fluids* 27:1974-1981. Doi: <https://doi.org/10.1063/1.864852>
- Bakewell HP, Lumley JL (1967) Viscous sublayer and adjacent wall region in turbulent pipe flow. *Phys Fluids* 10:1880-1889. Doi: <https://doi.org/10.1063/1.1762382>
- Berk T, Ganapathisubramani B (2000) Effects of vortex-induced velocity on the development of a synthetic jet issuing into a turbulent boundary layer. *J Fluid Mech* 870:651-679. Doi: <https://doi.org/10.1017/jfm.2019.279>
- Berk T, Hutchins N, Marusic I, Ganapathisubramani B (2018) Trajectory of a synthetic jet issuing into high-Reynolds-number turbulent boundary layers. *J Fluid Mech* 856:531-551. Doi: <https://doi.org/10.1017/jfm.2018.734>
- Chaudhry IA, Zhong S (2014) A single circular synthetic jet issued into turbulent boundary layer. *J Vis* 17:101-111. Doi: <https://doi.org/10.1007/s12650-014-0199-0>
- Chong MS, Perry AE, Cantwell BJ (1990) A general classification of three-dimensional flow fields. *Phys Fluids* 2:765-777. Doi: <https://doi.org/10.1063/1.857730>
- Fukagata K, Iwamoto K, Kasagi N (2002) Contribution of Reynolds stress distribution to the skin friction in wall-bounded flows. *Phys Fluids* 14:L73-L76. Doi: <https://doi.org/10.1063/1.1516779>
- Fukagata K, Kasagi N (2002) Highly energy-conservative finite difference method for the cylindrical coordinate system. *J Comput Phys* 181:478-498. Doi: <https://doi.org/10.1006/jcph.2002.7138>
- Fukagata K, Kasagi N (2003) Drag reduction in turbulent pipe flow with feedback control applied partially to wall. *Int J Heat Fluid Flow* 24:480-490. Doi: [https://doi.org/10.1016/S0142-727X\(03\)00058-4](https://doi.org/10.1016/S0142-727X(03)00058-4)
- Fukagata K, Kasagi N (2004) Suboptimal control for drag reduction via suppression of near-wall Reynolds shear stress. *Int J Heat Fluid Flow* 25:341-350. Doi: <https://doi.org/10.1016/j.ijheatfluidflow.2004.02.015>
- Gilarranz JL, Traub LW, Rediniotis OK (2002) Characterization of a compact, high-power synthetic jet actuator for flow separation control. *AIAA J* 6:127-155. Doi: <https://doi.org/10.2514/6.2002-127>
- Glezer A, Amitay M (2002) Synthetic jets. *Annu Rev Fluid Mech* 34:503-529. Doi: <https://doi.org/10.1146/annurev.fluid.34.090501.094913>
- Gomez T, Flutet V, Sagaut P (2009) Contribution of Reynolds stress distribution to the skin friction in compressible turbulent channel flows. *Phys Rev E* 79:035301. Doi: <https://doi.org/10.1103/PhysRevE.79.035301>
- Green MA, Rowley CW, Haller G (2007) Detection of Lagrangian coherent structures in three-dimensional turbulence. *J Fluid Mech* 572:111-120. Doi: <https://doi.org/10.1017/S0022112006003648>
- Guan X, Jiang N, Cheng L, Zhang H (2013) TRPIV measurement of turbulent coherent

- structures in a drag-reducing flow by polymers. *Theor App Mech Lett* 3:042006. Doi: <https://doi.org/10.1063/2.1304206>
- Haller G (2001) Distinguished material surfaces and coherent structures in three-dimensional fluid flows. *Physica D* 149:248-277. Doi: [https://doi.org/10.1016/S0167-2789\(00\)00199-8](https://doi.org/10.1016/S0167-2789(00)00199-8)
- Haller G, Yuan G (2000) Lagrangian coherent structures and mixing in two-dimensional turbulence. *Physica D* 147:352-370. Doi: [https://doi.org/10.1016/S0167-2789\(00\)00142-1](https://doi.org/10.1016/S0167-2789(00)00142-1)
- Hou YX, Somandepalli VSR, Mungal MG (2008) Streamwise development of turbulent boundary-layer drag reduction with polymer injection. *J Fluid Mech* 597:31-66. Doi: <https://doi.org/10.1017/S0022112007009718>
- Hunt JCR, Wray AA, Moin P (1988) Eddies, streams, and convergence zones in turbulent flows. Technical Report CTR-S88 N89-24555:193-208.
- Jeong J, Hussain F (1995) On the identification of a vortex. *J Fluid Mech* 285:69-94. Doi: <https://doi.org/10.1017/S0022112095000462>
- Kametani Y, Fukagata K (2011) Direct numerical simulation of spatially developing turbulent boundary layers with uniform blowing or suction. *J Fluid Mech* 681:154-172. Doi: <https://doi.org/10.1017/jfm.2011.219>
- Kendall A, Koochesfahani M (2008) A method for estimating wall friction in turbulent wall-bounded flows. *Exp Fluids* 44:773-780. Doi: <https://doi.org/10.1007/S00348-007-0433-9>
- Kim HT, Kline SJ, Reynolds WC (1971) The production of turbulence near a smooth wall in a turbulent boundary layer. *J Fluid Mech* 50:133-160. Doi: <https://doi.org/10.1017/S0022112071002490>
- Kim KC, Adrian RJ (1999) Very large-scale motion in the outer layer. *Phys Fluids* 11:417-422. Doi: <https://doi.org/10.1063/1.869889>
- Lardeau S, Leschziner MA (2011) The interaction of round synthetic jets with a turbulent boundary layer separating from a rounded ramp. *J Fluid Mech* 683:172-211. Doi: <https://doi.org/10.1017/jfm.2011.258>
- Lasagna D, Orazi M, Iuso G (2014) Streamwise vortices originating from synthetic jet-turbulent boundary layer interaction. *Fluid Dyn Res* 46:015501. Doi: <https://doi.org/10.1088/0169-5983/46/1/015501>
- Liepmann HW (1979) The rise and fall of ideas in turbulence: Research in turbulence, still the most difficult problem of fluid mechanics, continues to produce technological advances, but the path of progress is anything but straight. *Am Sci* 67:221-228. Doi: <https://www.jstor.org/stable/27849154>
- Lu L, Li D, Gao Z, Cao Z, Bai Y, Zheng J (2020) Characteristics of array of distributed synthetic jets and effect on turbulent boundary layer. *Acta Mech Sin* 36:1171-1190. Doi: <https://doi.org/10.1007/s10409-020-01001-x>
- Mathur M, Haller G, Peacock T, Felsot JER, Swinney HL (2007) Uncovering the Lagrangian skeleton of turbulence. *Phys Rev Lett* 98:144502. Doi: <https://doi.org/10.1103/PhysRevLett.98.144502>
- Mehdi F, White CM (2011) Integral form of the skin friction coefficient suitable for experimental data. *Exp Fluids* 50:43-51. Doi: <https://doi.org/10.1007/s00348-010->

- Min T, Kang SM, Speyer JL, Kim J (2006) Sustained sub-laminar drag in a fully developed channel flow. *J Fluid Mech* 588:309-318. Doi: <https://doi.org/10.1017/S0022112006000206>
- Park YS, Park SH, Sung HJ (2003) Measurement of local forcing on a turbulent boundary layer using PIV. *Exp Fluids* 34:697-707. Doi: <https://doi.org/10.1007/s00348-003-0604-2>
- Peet Y, Sagaut P (2009) Theoretical prediction of turbulent skin friction on geometrically complex surfaces. *Phys Fluids* 21:105105. Doi: <https://doi.org/10.1063/1.3241993>
- Rathnasingham R, Breuer KS (1997) Coupled fluid-structural characteristics of actuators for flow control. *AIAA J* 35:832-837. Doi: <https://doi.org/10.2514/2.7454>
- Rathnasingham R, Breuer KS (2003) Active control of turbulent boundary layers. *J Fluid Mech* 595:209-233. Doi: <https://doi.org/10.1017/jfm.2014.261>
- Robinson SK (1991) Coherent motions in the turbulent boundary layer. *Annu Rev Fluid Mech* 23:601-639. Doi: <https://doi.org/10.1146/annurev.fl.23.010191.003125>
- Sano M, Hirayama N (1985) Turbulent boundary layers with injection and suction through a slit. *Bulletin of JSME* 28:807-814. Doi: <https://doi.org/10.1299/jsme1958.28.807>
- Schlatter P, Orlu R (2010) Assessment of direct numerical simulation data of turbulent boundary layers. *J Fluid Mech* 659:116-126. Doi: <https://doi.org/10.1017/S0022112010003113>
- Shadden SC, Lekien F, Marsden JE (2005) Definition and properties of Lagrangian coherent structures from finite-time Lyapunov exponents in two-dimensional aperiodic flows. *Physica D* 212:271-304. Doi: <https://doi.org/10.1016/j.physd.2005.10.007>
- Shen J, Pan C, Wang J (2014) Accurate measurement of wall skin friction by single-pixel ensemble correlation. *Sci China Phys Mech* 57:1352-1362. Doi: <https://doi.org/10.1007/s11433-014-5462-9>
- Sirovich L, Kirby M, Winter M (1990) An eigenfunction approach to large scale transitional structures in jet flow. *Phys Fluids* 2:127-136. Doi: <https://doi.org/10.1063/1.857815>
- Smith BL, Glezer A (1998) The formation and evolution of synthetic jets. *Phys Fluids* 10:2281-2297. Doi: <https://doi.org/10.1063/1.869828>
- Sugiyama K, Calzavarini E, Lohse D (2008) Microbubbly drag reduction in Taylor-Couette flow in the wavy vortex regime. *J Fluid Mech* 608:21-41. Doi: <https://doi.org/10.1017/S0022112008001183>
- Suponitsky V, Cohen J, Yoseph PZB (2005) The generation of streaks and hairpin vortices from a localized vortex disturbance embedded in unbounded uniform shear flow. *J Fluid Mech* 535:65-100. Doi: <https://doi.org/10.1017/S0022112005004453>
- Tang Z, Jiang N (2012) Dynamic mode decomposition of hairpin vortices generated by a hemisphere protuberance. *Sci China Phys Mech* 55:118-124. Doi:

- <https://doi.org/10.1007/s11433-011-4535-2>
- Voth GA, Porta AL, Crawford AM, Alexander J, Bodenschatz E (2002) Measurement of particle accelerations in fully developed turbulence. *J Fluid Mech* 469:121-160. Doi: <https://doi.org/10.1017/S0022112002001842>
- Westerweel J, Geelhoed PF, Lindken R (2004) Single-pixel resolution ensemble correlation for micro-PIV applications. *Exp Fluids* 37:375-384. Doi: <https://doi.org/10.1007/s00348-004-0826-y>
- Wu Y, Christensen KT (2010) Spatial structure of a turbulent boundary layer with irregular surface roughness. *J Fluid Mech* 655:380-418. Doi: <https://doi.org/10.1017/S0022112010000960>
- Xu C, Deng B, Huang W, Cui G (2013) Coherent structures in wall turbulence and mechanism for drag reduction control. *Sci China Phys Mech* 56:1053-1061. Doi: <https://doi.org/10.1007/s11433-013-5087-4>
- Xu J, Dong S, Maxey MR, Karniadakis GE (2007) Turbulent drag reduction by constant near-wall forcing. *J Fluid Mech* 582:79-101. Doi: <https://doi.org/10.1017/S0022112007005460>
- Yang S, Jiang N (2012) Tomographic TR-PIV measurement of coherent structure spatial topology utilizing an improved quadrant splitting method. *Sci China Phys Mech* 55:1863-1872. Doi: <https://doi.org/10.1007/s11433-012-4887-2>
- Ye Z, Jiang Y, Zhang Y, Zou J, Zheng Y (2019) Effects of synthetic jet array on turbulent boundary layer. *Int J Heat Technol* 37:893-898. Doi: <https://doi.org/10.18280/ijht.370327>
- Yu B, Li F, Kawaguchi Y (2004) Numerical and experimental investigation of turbulent characteristics in a drag-reducing flow with surfactant additives. *Int J Heat Fluid Flow* 25:961-974. Doi: <https://doi.org/10.1016/j.ijheatfluidflow.2004.02.029>
- Zhou J, Adrian RJ, Balachandar S, Kendall TM (1999) Mechanisms for generating coherent packets of hairpin vortices in channel flow. *J Fluid Mech* 387:353-396. Doi: <https://doi.org/10.1017/S002211209900467X>